Int. J. Heat Mass Transfer. Vol. 34, No. 8, pp. 2107–2121, 1991
Printed in Great Britain

0017–9310/91 $3.00 + 0.00

Numerical modeling of solidification and convection in a viscous pure binary eutectic system

CURTIS M. OLDENBURG and FRANK J. SPERA

Department of Geological Sciences and Institute for Crustal Studies, University of California, Santa Barbara, Santa Barbara, CA 93106, U.S.A.

(*Received* 30 *April* 1990 *and in final form* 2 *October* 1990)

Abstract—The solidification and convection of the pure binary eutectic silicate system diopside–anorthite (Di–An) is numerically modeled. A mass-weighted enthalpy of fusion is used to account for the second solid phase (An) which crystallizes at the solidus temperature. Variable under-relaxation is used to aid convergence of the momentum equations in our implementation of the SIMPLER algorithm used to solve the two-dimensional continuum conservation equations. Numerical experiments of the solidification of Di80 melt show that a large temperature drop occurs across the solid and mush regions which decreases convective vigor in the liquid. Interesting compositional segregation patterns are produced during the solidification of Di80.

1. INTRODUCTION

MUCH PROGRESS has been made recently in the numerical modeling of solidification and convection in systems of metallurgical interest by the development of single-region continuum models readily amenable to numerical solution [1–3]. Meanwhile numerical modeling of phase change and convection in geological systems has received much less attention despite the fact that solidification and convection are fundamental processes in magmatic evolution. Because the single-region continuum models developed for metallurgical application are general, they can be used with some modifications to model silicate melt. The recent studies of solidification and convection in metallurgical systems provide the framework for studies of heat transfer and convective dynamics associated with the cooling and solidification of magma bodies.

The focus of this paper is on solidification and convection of silicate melt. We have selected for consideration the diopside–anorthite (Di–An) pure binary eutectic system for its relevance to the evolution of basaltic magma, the most abundant magma on earth. We present a model and results from the numerical code developed for phase change and convection in this viscous pure binary eutectic system. Numerical simulations of previously published cases of metallurgical interest verify the accuracy of the model and the numerical code. An example numerical experiment of phase change and convection in Di–An demonstrates the capabilities of the model. The ultimate goal of these studies is the understanding of the processes of phase change and convection and their effects on the thermal and compositional evolution of planetary magmatic systems.

2. REVIEW OF PRIOR WORK

2.1. *Materials science*

Several single-region models of solidification and convection in systems of metallurgical interest have been put forward in recent years [1–3]. The equations in single-region models are valid over the entire solution domain and obviate phase interface tracking as required in multi-region models. Single-region formulations have proven convenient because of their amenability to solution by the SIMPLER algorithm, a primitive variable, iterative, control-volume finite difference algorithm [4, 5].

The derivation of the continuum formulation of Bennon and Incropera [1] is based on classical mixture theory. The momentum equations are written for the mixture velocities, relying on the value of the permeability in each control volume (a function of the fraction solid through the Blake–Kozeny–Carman relation) to determine whether flow through porous mush is important in that control volume. The assumption of local thermodynamic equilibrium is made implying: (1) all phases within a control volume are at the same temperature; (2) the compositions of the solid and liquid coexisting in the control volume are determined by the phase diagram; and (3) the lever rule determines the relative proportions of solid and liquid present in the control volume. The capabilities and limitations of the formulation have been shown through modeling solidification and convection in the system NH_4Cl–H_2O [6], and comparisons of numerical and laboratory results [7].

Volume-averaging is used by Beckermann and Viskanta [2] to arrive at single-region equations similar to those of Bennon and Incropera [1]. The momentum equation is written in terms of the velocity of the

NOMENCLATURE

A	difference, $h^*_{liq} - h_{sol}$
C	composition
c_p	heat capacity
d	depth of domain
D	chemical diffusivity
Da	Darcy number
g	acceleration of gravity
h	enthalpy
h^*_{liq}	projection of h_{liq} to T_{sol}
j	species flux
k	thermal conductivity
K	permeability
L	width of domain
Le	Lewis number
n	iteration number
p	pressure
q	heat flux
R	ramp slope parameter
Ra	thermal Rayleigh number
Rs	compositional Rayleigh number
S	source term
St	Stefan number
t	time
T	temperature
u	horizontal velocity
v	vertical velocity
$\mathbf{v}$	velocity vector
x	horizontal coordinate
y	vertical coordinate.

Greek symbols

α	coefficient of isobaric thermal expansion
α_u	ramp under-relaxation parameter
β	coefficient of compositional expansion
κ	thermal diffusivity
μ	dynamic viscosity
ν	kinematic viscosity
ρ	density
ϕ	general field variable
ψ	stream function.

Subscripts

eut	eutectic
f	fusion
i	initial
l	liquid
liq	liquidus
m	pure end-member
r	ratio
s	solid
s1	solid 1 (diopside)
s2	solid 2 (anorthite)
sol	solidus
w	wall
0	reference value.

Superscript

^	dimensionless variables.

liquid and reduces to the appropriate form depending on the value of the fraction solid. Local thermodynamic equilibrium and the lever rule are used to relate temperature, composition, and fraction solid within a control volume. Beckermann and Viskanta [2] present a direct comparison of numerical vs laboratory results which points out the challenge of modeling processes such as solidification and convection which occur over a large range of length scales.

A two-phase model was proposed by Voller *et al.* [3]. In this formulation, momentum equations are written for each of the phases, solid and liquid, with source terms to account for phase interaction. Enthalpy and species equations are also written for both phases, and appropriate interphase terms attached. An example case where there is no distinction between phases in the mush (i.e. the mush region is treated as a single pseudo-fluid) and two different illustrative cases of models with distinct phases in the mush (dispersed microstructure and distinct microstructure) were compared. The conclusion that different limiting cases of the model are appropriate in different limiting physical situations is a useful reminder that the realm of applicability of the various models must be understood when modeling phase change and convection.

2.2. *Geological sciences*

The study of crystallization in an aqueous sodium carbonate solution by Thompson and Szekely [8] spans the gap between materials science and geology in terms of numerical modeling of phase change and convection in so far as crystallizing aqueous systems have been used in the past as analogs to magma bodies [9, 10]. The work of Smith [11] considers the effect of solidifying magma on convective instability and vigor by linear stability analysis and in one dimension (see also, Marsh [12]). The model of Worster *et al.* [13] includes important kinetic effects on the crystallization of melts in the Di–An system, but its simplified one-dimensional approach does not elucidate the flow field.

Other prior numerical studies of magmatic convection have assumed single-phase convection [14] or they have modeled the effects of solidification on the composition field heuristically by defining a flux-type boundary condition which crudely models the production of light component during solidification of

magma [15]. In these models, sidewall and bottom or top thermal and compositional boundary conditions must be arbitrarily chosen as either Dirichlet (constant values of temperature or composition) or Neumann (constant fluxes of heat or mass) [16]. In fact, the boundary between magma and the sidewall is gradational from relatively fluid magma in the interior, to mush, to fully solidified magma along the cold wall. The interface between mush which is too viscous to convect and more fluid magma constitutes a rheological sidewall. The thermal boundary conditions at this sidewall are influenced by the liberation or consumption of latent heat due to local phase change. This sidewall, the boundary between what is effectively a solid phase and the liquid magma, moves as solidification proceeds and its location is part of the solution of the continuum solidification equations. Thus continuum solidification models eliminate the necessity of choosing arbitrary boundary conditions at the solid–melt interface, as the boundary between magma and solid rock is part of the solution.

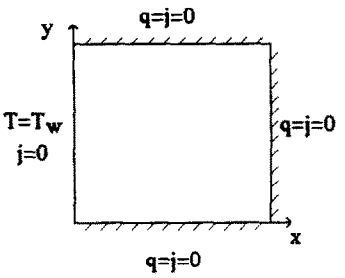

FIG. 1. Domain and boundary conditions for calculations of solidification and convection. The domain is 1×1, rigid, impermeable, and insulated on three sides. The left-hand sidewall is held at T_w.

3. DIFFERENCES BETWEEN METALLURGICAL AND GEOLOGICAL SYSTEMS

3.1. *Physical environment*

Magma bodies are large regions (volume up to 10^4 km^3) of molten and partially-molten rock (usually silicate melt) underlying active volcanic areas in continental or oceanic crust at depths generally greater than 2 km. Seismic investigations [17], surface heat flow measurements [18], and explosive eruptions of predominantly liquid magma [19] provide substantial evidence for the existence of magma bodies. Typical dimensions of magma bodies are of the order of 10^2–10^4 m, whereas length scales of containers in metallurgical systems are much smaller (10^{-3}–10^0 m).

Varied conditions in the earth's crust give rise to a great range of dynamic processes which can occur in magma bodies from solidification to melting, stagnation to vigorous convection, and thermal and chemical isolation to strong connectivity to sources of magma below. Similar ranges of processes occur in metallurgical applications, but there the processes of heating and cooling are controlled in the laboratory. Conversely, magma occupies chambers with poorly understood boundary conditions and connectivity with deeper sources of magma all of which can change with time. Because of the large range of potentially applicable boundary conditions, we adopt in this study for illustrative purposes a simplified model domain in which cooling occurs primarily through the sidewall and is thermally and chemically disconnected from sources below. The model domain is shown along with boundary conditions in Fig. 1. The left-hand wall is held at a subsolidus temperature while all other boundaries are adiabatic. All sides of the body are impermeable (no mass flux) and rigid. The objective of the present study is to model phase change and convection of silicate melt in the case of sidewall cooling. Future studies may consider more realistic boundary conditions relative to natural magmatic systems. Because of practical limits on the magnitude of the Rayleigh number in present computational studies, the model domain studied is nowhere near the dimensions of an actual magma body. We shall have to wait for improvements in both computational speed and memory as well as algorithms to tackle the problem of high-Rayleigh number convection which is associated with large magma bodies.

3.2. *Physical properties*

There are two main features of systems of metallurgical interest which distinguish them from situations of phase change and convection in basaltic magmatic systems: (1) binary phase diagrams for systems in metallurgy commonly involve a significant range of solid solution whereas the Di–An system is pure binary eutectic in character; (2) the viscosities of liquid metals are very small and the thermal diffusivities are very large in comparison with silicate melts at near-liquidus temperatures making the Prandtl number (Pr) vastly different in the two cases (typical basaltic magma has $Pr = 10^3$, while liquid metals have $Pr = 10^{-2}$). It is important to note that smaller viscosity affects not only momentum transport through Pr but also crystal nucleation and growth rates (not considered here) which can profoundly affect crystal morphology. We have accommodated the pure binary eutectic phase diagram which is applicable to the solidification of basaltic magma through definition of an effective heat of fusion to be discussed in the next section. While the continuum models put forward recently have sufficient generality to accommodate the large viscosity of silicates in theory, practical computational difficulties in calculating momentum transport can arise from the large Prandtl number of silicate melt. This difficulty requires modification of the usual numerical scheme successful in low-Prandtl number systems and will be discussed in a later section.

4. PURE BINARY EUTECTIC SYSTEM DIOPSIDE–ANORTHITE

4.1. *Properties and the effective heat of fusion*

The model silicate system we have chosen is the diopside–anorthite (Di–An) pure binary eutectic system for which the thermophysical properties are given in Table 1. The Di–An system approximates basalt of which about 20 km^3 solidifies each year, mostly along mid-ocean ridge spreading centers [20]. Figure 2 shows the phase diagram for Di–An with the liquidi linearized to simplify the lever-rule phase relations. A bulk composition of Di80 at $T = 1337$ °C was chosen as the bulk initial composition and temperature for the example numerical experiment, while the left-hand wall is held at a subsolidus temperature, $T = 1265$ °C. The thermophysical properties of Di80 are given in Table 2. It should be noted that the viscosity of silicate melts is temperature and composition dependent [21]. The continuum model enables the inclusion of these effects. However, for simplicity in the present study, we have assumed a constant liquid viscosity.

Table 1. Thermophysical properties of diopside and anorthite

Property	Units	Values Di	An
T_{liq}	K	1665	1830
T_{sol}	K	1548	1548
h_f	10^5 J kg^{-1}	3.574	2.914
ρ	kg m^{-3}	2651	2562

References [32, 33].

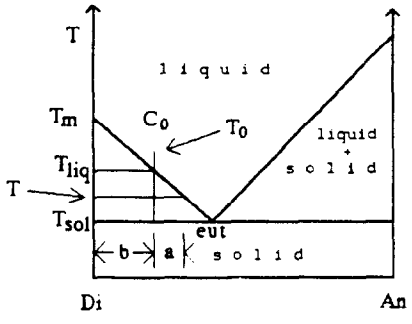

FIG. 2. Diopside–anorthite (Di–An) pure binary eutectic phase diagram. Thermophysical properties are given in Table 1. The initial composition, C_0, is Di80. As shown, at any given T between T_{liq} and T_{sol}, the fraction solid is given by the ratio $a/(a+b)$. Below T_{sol}, a mixed solid of Di80 composition exists.

Table 2. Assumed thermophysical properties of Di80

Property	Units	Value
T_{liq}	K	1606
T_{sol}	K	1548
c_p	J kg^{-1} K^{-1}	1006
κ	m^2 s^{-1}	10^{-6}
D	m^2 s^{-1}	10^{-8}
μ	m kg^{-1} s^{-1}	3.6†
α	K^{-1}	10^{-5}
β	—	10^{-2}

† Reference [21] at $T = 1610$ K.

Briefly, the behavior of the system is as follows. First, as heat flows out of the left-hand wall, solidification occurs along the wall. The first solid formed is pure Di. Where the temperature is between the solidus and liquidus, pure Di coexists with liquid. At any location where the temperature is below the solidus, such as along the left-hand wall, a mixed solid of composition 80% Di and 20% An is present. At the solidus temperature, there can be liquid, pure Di, and a mixed solid of eutectic composition (Di60), depending on the local value of enthalpy. The proportions of liquid, pure Di and the mixed solid of eutectic composition (Di60) change in each control volume as the enthalpy decreases until the point at which melt is gone and the solid remaining is a mixed solid of Di80 composition.

The energetics of a second solid phase (pure An) are treated by defining a mixed solid of eutectic composition (Di60) with a corresponding mass-weighted effective heat of fusion equal to

$$h_f^* = 0.60h_{fDi} + 0.40h_{fAn} \quad (1)$$

which gives an effective heat of fusion (h_f^*) of 3.31×10^5 J kg^{-1}. This approximation is valid because of the similarity of the heat capacities of the two silicate end-members (Table 3). That is, compared to the differences in heats of fusion, the differences in heat capacities of the two end-members can be neglected. The different heats of fusion are considered explicitly by mass averaging the heats of fusion of Di and An. This differs from prior studies of metallurgical systems where solid solution occurs and results in a single solid phase at subsolidus tem-

Table 3. Heat capacities of diopside and anorthite

Units	Di T_{liq} (= 1665 K)	Di T_{sol} (= 1548 K)	An T_{liq} (= 1830 K)	An T_{sol} (= 1548 K)
J kg^{-1} K^{-1}	1235	1000	1300	1028

References [32, 33].

peratures and thus involves only one solid and one heat of fusion at subsolidus temperatures.

5. MODEL EQUATIONS

5.1. *Differential equations*

The continuum phase change and convection equations for an incompressible fluid in two-dimensions are [1]

$$\frac{\partial u}{\partial x}+\frac{\partial v}{\partial y}=0 \tag{2}$$

$$\rho_0\left(\frac{\partial u}{\partial t}+u\frac{\partial u}{\partial x}+v\frac{\partial u}{\partial y}\right)=-\frac{\partial p}{\partial x}+\frac{\partial}{\partial x}\left(\mu\frac{\partial u}{\partial x}\right)+\frac{\partial}{\partial y}\left(\mu\frac{\partial u}{\partial y}\right)-\frac{\mu}{K_x}(u-u_s) \tag{3}$$

$$\rho_0\left(\frac{\partial v}{\partial t}+u\frac{\partial v}{\partial x}+v\frac{\partial v}{\partial y}\right)=-\frac{\partial p}{\partial y}+\frac{\partial}{\partial x}\left(\mu\frac{\partial v}{\partial x}\right)+\frac{\partial}{\partial y}\left(\mu\frac{\partial v}{\partial y}\right)-\rho g-\frac{\mu}{K_y}(v-v_s) \tag{4}$$

$$\left(\frac{\partial h}{\partial t}+u\frac{\partial h}{\partial x}+v\frac{\partial h}{\partial y}\right)=\frac{\partial}{\partial x}\left(\kappa\frac{\partial h}{\partial x}\right)+\frac{\partial}{\partial y}\left(\kappa\frac{\partial h}{\partial y}\right)+\frac{\partial}{\partial x}\left(\kappa\frac{\partial(h_s-h)}{\partial x}\right)+\frac{\partial}{\partial y}\left(\kappa\frac{\partial(h_s-h)}{\partial y}\right)-\left(\frac{\partial(h_l-h)(u-u_s)}{\partial x}\right)-\left(\frac{\partial(h_l-h)(v-v_s)}{\partial y}\right) \tag{5}$$

$$\left(\frac{\partial C}{\partial t}+u\frac{\partial C}{\partial x}+v\frac{\partial C}{\partial y}\right)=\frac{\partial}{\partial x}\left(D\frac{\partial C}{\partial x}\right)+\frac{\partial}{\partial y}\left(D\frac{\partial C}{\partial y}\right)+\frac{\partial}{\partial x}\left(D\frac{\partial(C_l-C)}{\partial x}\right)+\frac{\partial}{\partial y}\left(D\frac{\partial(C_l-C)}{\partial y}\right)-\left(\frac{\partial(C_l-C)(u-u_s)}{\partial x}\right)-\left(\frac{\partial(C_l-C)(v-v_s)}{\partial y}\right) \tag{6}$$

where symbols are as defined in the Nomenclature. It is assumed that the density obeys the relation

$$\rho=\rho_0(1-\alpha(T-T_{sol})-\beta(C-C_{sl})) \tag{7}$$

where T_{sol} is 1275°C and C_{sl} is pure Di. It is further assumed that density changes are important only in the body force term (i.e. the Boussinesq approximation is valid) and that the viscosity can be a function of T or C (but is assumed constant here (i.e. $\mu=\mu_0$, and $\mu_r=\mu/\mu_0=1$ in equations (9)–(13) below)).

The above equations (2)–(6) are appropriate for systems in which the liquid phase flows through the porous mush in the two-phase solid–liquid region [1]. The last terms on the right-hand side of equations (3) and (4) are the Darcy flow terms; the last terms on the right-hand side of equations (5) and (6) are the interphase transport terms. These terms account for the flow of liquid through the porous mush and the associated interphase transport of heat and chemical species. The full equations (2)–(6) constitute the relative motion (RM) model. For systems such as waxes in which the solid phase is indistinguishable from the liquid phase and thus there is no relative motion between melt and solid, one can define a viscosity function based on the fraction solid (see recommendation of Metzner [22]) and omit the Darcy flow terms in equations (3) and (4) and the interphase transport terms in equations (5) and (6). The reduced set of equations constitutes the no-relative motion (NRM) model.

Prior studies [1, 2] used the Blake–Kozeny–Carman equation to relate the permeability to the fraction solid (f_s) for all values of f_s in the RM model

$$K=K_0\left(\frac{(1-f_s)^3}{f_s^2}\right). \tag{8}$$

We adopt here the same formulation. However, it should be noted that the flow in dilute mush (where liquid is the connected phase) and the flow in concentrated mush (where solid is the connected phase) are different. Specifically, flow of dilute mush can be more accurately modeled as a two-phase fluid the viscosity of which increases as the fraction of solid (f_s) increases. The flow in concentrated mush is accurately modeled by Darcy's law with permeability represented by equation (8) for laminar flow. Explicit consideration of the differences between flow in dilute mush and in concentrated mush gives rise to a hybrid model. Results of our hybrid model, which combines the viscosity dependence on f_s in dilute mush (through the equation recommended by Metzner [22]) and the permeability dependence on f_s in concentrated mush (through the Blake–Kozeny–Carman equation), have been presented elsewhere [23]. In the present study, we consider the standard RM model consistent with prior work in materials science.

Introducing the following scales:

$$\hat{x}=\frac{x}{L},\quad \hat{y}=\frac{y}{L},\quad \hat{u}=\frac{uL}{\kappa},\quad \hat{v}=\frac{vL}{\kappa}$$

$$\hat{p}=\frac{L^2}{\mu_0\kappa}p,\quad \hat{t}=t\frac{\kappa}{L^2}St$$

and the following definitions of dimensionless groups:

$$\hat{h}=\frac{(h-h_{sol})}{(h^*_{liq}-h_{sol})},\quad \hat{h}_s=\frac{(h_s-h_{sol})}{(h^*_{liq}-h_{sol})},\quad \hat{h}_l=\frac{(h_l-h_{sol})}{(h^*_{liq}-h_{sol})}$$

$$\hat{T}=\frac{(T-T_{sol})}{(T_0-T_{sol})},\quad \hat{C}=\frac{(C-C_{sl})}{(C_{s2}-C_{sl})},\quad \hat{C}_l=\frac{(C_l-C_{sl})}{(C_{s2}-C_{sl})}$$

$$Pr=\frac{\nu_0}{\kappa},\quad Ra=\frac{g\alpha(T_0-T_{sol})L^3}{\kappa\nu_0}$$

$$Rs=\frac{g\beta(C_{s2}-C_{sl})L^3}{\kappa\nu_0},\quad St=\frac{C_p(T_0-T_{sol})}{(h^*_{liq}-h_{sol})}$$

$$Le=\frac{\kappa}{D},\quad Da=\frac{K_0}{L^2}$$

the equations are put into dimensionless form where hats have been suppressed

$$\frac{\partial u}{\partial x}+\frac{\partial v}{\partial y}=0 \tag{9}$$

$$\frac{1}{Pr}\left(St\frac{\partial u}{\partial t}+u\frac{\partial u}{\partial x}+v\frac{\partial u}{\partial y}\right)=-\frac{\partial p}{\partial x}+\frac{\partial}{\partial x}\left(\mu_r\frac{\partial u}{\partial x}\right)+\frac{\partial}{\partial y}\left(\mu_r\frac{\partial u}{\partial y}\right)-\frac{\mu_r K_0}{Da\,K_x}(u-u_s) \tag{10}$$

$$\frac{1}{Pr}\left(St\frac{\partial v}{\partial t}+u\frac{\partial v}{\partial x}+v\frac{\partial v}{\partial y}\right)=-\frac{\partial p}{\partial y}+\frac{\partial}{\partial x}\left(\mu_r\frac{\partial v}{\partial x}\right)+\frac{\partial}{\partial y}\left(\mu_r\frac{\partial v}{\partial y}\right)+Ra\cdot T+Rs\cdot C-\frac{\mu_r K_0}{Da\,K_y}(v-v_s) \tag{11}$$

$$St\frac{\partial h}{\partial t}+u\frac{\partial h}{\partial x}+v\frac{\partial h}{\partial y}=\frac{\partial}{\partial x}\left(\frac{\partial h}{\partial x}\right)+\frac{\partial}{\partial y}\left(\frac{\partial h}{\partial y}\right)+\frac{\partial}{\partial x}\left(\frac{\partial(h_s-h)}{\partial x}\right)+\frac{\partial}{\partial y}\left(\frac{\partial(h_s-h)}{\partial y}\right)-\left(\frac{\partial(h_l-h)(u-u_s)}{\partial x}\right)-\left(\frac{\partial(h_l-h)(v-v_s)}{\partial y}\right) \tag{12}$$

$$St\frac{\partial C}{\partial t}+u\frac{\partial C}{\partial x}+v\frac{\partial C}{\partial y}=\frac{\partial}{\partial x}\left(\frac{1}{Le}\frac{\partial C}{\partial x}\right)+\frac{\partial}{\partial y}\left(\frac{1}{Le}\frac{\partial C}{\partial y}\right)+\frac{\partial}{\partial x}\left(\frac{1}{Le}\frac{\partial(C_l-C)}{\partial x}\right)+\frac{\partial}{\partial y}\left(\frac{1}{Le}\frac{\partial(C_l-C)}{\partial y}\right)-\left(\frac{\partial(C_l-C)(u-u_s)}{\partial x}\right)-\left(\frac{\partial(C_l-C)(v-v_s)}{\partial y}\right). \tag{13}$$

Although several classical dimensionless numbers appear in the equations above, their significance is slightly different in phase-change systems from that in single-phase systems. For example, the thermal Rayleigh number (Ra) gives an indication of the importance of thermal buoyancy effects relative to viscous effects in natural convection; the compositional Rayleigh number (Rs) gives the analogous relation for compositional buoyancy. Nevertheless, the convective heat transfer cannot be accurately related to Ra in a scaling relation (as done by Roberts [24] for single-phase convection) when Ra is based on the width of the whole domain because for much of the solidification evolution only a small part of the domain contains liquid capable of convection. The Lewis number (Le) is the ratio of thermal to chemical diffusivity and thus provides an indication of the ratio of thermal boundary layer thickness to chemical boundary layer thickness. However, since chemical diffusivity is a function of the fraction solid in this continuum model (i.e. diffusion in the solid is negligible compared to diffusion in the melt), scaling relations for boundary layer thicknesses using Le can only be applied in pure liquid regions. The Prandtl number (Pr) indicates the importance of inertia to viscous effects and, in the NRM model, should only be applied in pure liquid regions. The Stefan number (St) indicates the magnitude of superheat relative to the heat of fusion. In the model problem considered here, the amount of superheat goes to zero as the system solidifies. The Darcy number (Da) is only relevant in regions where solid is present and plays no role in the pure liquid region. It should further be noted that other quantities (e.g. Table 7) and the form of the phase diagram (Fig. 2) enter into phase change problems in addition to the above classical dimensionless numbers.

5.2. *Additional equations*

Supplementary equations are required to relate the enthalpy to temperature, the temperature to fraction solid, and the phase compositions to fraction solid. With reference to the generalized enthalpy–temperature diagram (Fig. 3), and assuming local thermodynamic equilibrium, the dimensional equations in Table 4 relate the temperature (T) and fraction solid (f_s) to enthalpy (h) depending on the enthalpy at any given location in the pure binary eutectic model.

In general, the enthalpy of the mixture (h) is given in terms of the enthalpy of the solid (h_s), the enthalpy of the liquid (h_l), and the fraction solid (f_s) by

$$h=f_s h_s+(1-f_s)h_l \tag{14}$$

where

$$h_s=C_p T \tag{15}$$

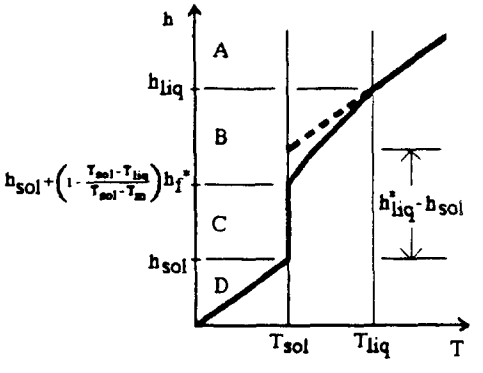

FIG. 3. Enthalpy–temperature diagram showing the four regions (A, B, C, D) of different h–f_s–T relations. h^*_{liq} is the projection of the superliquidus enthalpy down to T_{sol}. h_f^* is the mass-weighted heat of fusion of the mixed solid of Di60 composition. $h^*_{liq}-h_{sol}$ is the enthalpy scale in the Stefan number. Between T_{sol} and T_{liq}, one uses h_f (the heat of fusion of diopside) for the source term which accounts for release of latent heat. At T_{sol}, the mass-weighted heat of fusion (h_f^*) is used to account for enthalpy produced during the formation of diopside and anorthite which solidify in eutectic proportions.

Table 4. Relations between enthalpy (h), fraction solid (f_s), and temperature (T) in the pure binary eutectic model in the four different regions of Fig. 3

Region	f_s	T
A	0	$\frac{h-(h^*_{liq}-h_{sol})}{c_p}$
B	root of equation (18)	$\frac{T_{liq}-T_m f_s}{1-f_s}$
C	$1-\frac{h-h_{sol}}{h_f^*}$	T_{sol}
D	1	$\frac{h}{c_p}$

and

$$h_l = C_p T + h^*_{liq} - h_{sol} \tag{16}$$

and where it is assumed that there is only one heat capacity (c_p) in the system, a reasonable approximation for Di–An (Table 3) and most silicate systems. The term h^*_{liq} is simply the projection of the superliquidus enthalpy curve down to T_{sol}.

The temperature in subsolidus and superliquidus regions (D and A, respectively) is linearly related to h through the heat capacity (c_p) (Fig. 3). In regions D and A, f_s is unity and zero, respectively.

In supersolidus and subliquidus region B of Fig. 3, f_s is given by

$$f_s = \frac{T-T_{liq}}{T-T_m}. \tag{17}$$

Substituting equations (15)–(17) into equation (14) and simplifying, we arrive at the equation giving the enthalpy of the mixture in terms of f_s for region B

$$h = \left(\frac{A}{1-f_s}\right) f_s^2 - \left(\frac{2A-c_p T_m}{1-f_s}\right) f_s + \left(\frac{c_p T_{liq}+A}{1-f_s}\right) \tag{18}$$

where

$$A = h^*_{liq} - h_{sol}. \tag{19}$$

Equation (18) is valid where the fraction solid (f_s) does not exceed the value obtained when T just reaches T_{sol} (i.e. $f_s < (T_{liq}-T_{sol})/(T_m-T_{sol})$) during cooling in region B. Newton–Raphson iteration is used to solve equation (18) for fraction solid given enthalpy. The T–f_s relation in region B is given by equation (17) or, equivalently, as shown in Table 4.

In supersolidus region C where $1 > f_s \geqslant (T_{liq}-T_{sol})/(T_m-T_{sol})$, a simple linear relation using the enthalpy of fusion of the eutectic mixed solid (h_f^*) is used to calculate f_s.

Additional equations relate phase compositions and mixture properties to those of the particular phases in the pure binary eutectic model with an immobile solid phase:

for $f_s < \frac{T_{liq}-T_{sol}}{T_m-T_{sol}}$

$$C = (1-f_s)C_l \tag{20}$$

for $f_s \geqslant \frac{T_{liq}-T_{sol}}{T_m-T_{sol}}$

$$C = f_s\left(f_s - \frac{T_{liq}-T_{sol}}{T_m-T_{sol}}\right) C_{eut} + (1-f_s)C_{eut} \tag{21}$$

$$\mathbf{v} = (1-f_s)\mathbf{v}_l \tag{22}$$

$$D = (1-f_s)D_l. \tag{23}$$

The derivation of equation (21) is presented in the Appendix.

6. SOLUTION METHODOLOGY

6.1. *General method*

Each of the differential equations can be cast into the general form

$$\frac{\partial(\rho\phi)}{\partial t} + u\frac{\partial(\rho\phi)}{\partial x} + v\frac{\partial(\rho\phi)}{\partial y} = \frac{\partial}{\partial x}\left(\Gamma_\phi \frac{\partial\phi}{\partial x}\right) + \frac{\partial}{\partial y}\left(\Gamma_\phi \frac{\partial\phi}{\partial y}\right) + S_\phi \tag{24}$$

where ϕ denotes any one of the dependent variables of the mixture. The source term S accounts for the Darcy flow and body force terms in the momentum equations, the source of latent heat and relative phase motion in the energy equation, and the source of species and relative phase motion in the species equation. Each of the individual terms of the differential equations (9)–(13) can be put into the general form above. These terms have been set down by Bennon and Incropera [1, 25] to which we refer the reader for explicit details and exceptionally clear discussion. Once in this general form, the equations are amenable to solution by the primitive variable, control-volume-based, iterative finite difference SIMPLER algorithm [4, 5, 26, 27]. The use of primitive variables (u, v, and p) allows the direct extension to three dimensions.

In our implementation of the SIMPLER algorithm, we have used a standard tridiagonal matrix solver (Thomas algorithm) for line traverses in the x- and y-directions while doing sweeps alternately left to right and then bottom to top over the domain. To improve the convergence of the sweeps with the Thomas algorithm, we use improved off-line values as defined in enhancement number 5 of Van Doormaal and Raithby [28]. Five sweeps in the x- and y-directions are carried out for the momentum, enthalpy and composition equations. For the pressure equations, sweeps are carried out until the residual, defined by the degree to which the pressure equation is satisfied, is reduced to a certain small fraction of its value at

the beginning of the sweeps (this is enhancement number 6 of Van Doormaal and Raithby [28]). About 20–50 sweeps of the pressure equation are typically required to reduce the residual to a given small fraction of its initial value. In order to properly consider the fluxes in the continuum formulation as explained by Bennon and Incropera [25], upwinding is used to treat advective terms rather than the power-law scheme. The discretized equations are solved over a uniform rectangular, staggered mesh. The supplementary relations and Newton–Raphson iteration for finding the fraction solid from the enthalpy, where necessary, are performed at each iteration.

6.2. *Difficulty of high Pr convection*

The poor convergence properties of control-volume-based, iterative, finite difference schemes at large Rayleigh (Ra) and Prandtl (Pr) numbers are well documented [29]. The difficulty arises because of the strong bi-directional coupling between the energy and momentum equations which arises in natural convection when Pr is large. In natural convection, there is always a strong one-way coupling from the energy equation to the momentum equation which is controlled by the magnitude of Ra through the body force term. This one-way coupling causes no problems in iterative methods. To understand the bi-directional coupling problem intuitively, assume for the moment that the magnitude of Pr is controlled solely by the thermal diffusivity. If thermal diffusivity is very large, Pr is small and the energy equation is diffusion dominated. In this case, the momentum equation does not feed back into the energy equation significantly since advection terms in the energy equation are not important relative to diffusion terms. In this case, there is one-way coupling from the energy equation to the momentum equation through the body force terms and convergence is facilitated. Conversely, when thermal conductivity is small, Pr is large and advection terms are important in the energy equation. The energy to momentum equation coupling still exists through the body force term, but now there is also strong momentum to energy equation coupling through the advection terms in the energy equation. This constitutes bi-directional coupling which impedes convergence of the iterative method [29].

Convergence rates in natural convection at large Pr and Ra can be improved if the bi-directional coupling between the energy and momentum equations can be decreased. The magnitudes of Ra and Pr in the physical system being modeled control the initial coupling, but the use of variable under-relaxation within a time step can vastly increase convergence rates. In general, the technique we have used involved using progressively smaller values for the under-relaxation parameters in the momentum equation. This progressively decouples the momentum equation from the energy equation and leads to faster convergence. Specifically, a ramp under-relaxation function is defined as follows:

$$\alpha_u = \alpha_{ui}\, e^{-Rn} \tag{25}$$

where α_u and α_{ui} are the current and initial momentum under-relaxation parameters, respectively, R determines the slope of the ramp, and n the iteration number. Variable under-relaxation begins after five iterations with α_{ui} as the under-relaxation parameter. A slope value of 0.7 for R provided sufficient decoupling for reasonable convergence rates.

6.3. *Convergence criteria*

The convergence of the momentum equations is governed by the satisfaction of the continuity equation (conservation of mass, equation (9)) in each control volume. It is important to note that the convergence criterion for the momentum equations is absolute and based on the close satisfaction of the continuity equation and not on relative changes in velocity. No false convergence is caused by the ramp under-relaxation technique; at iterative convergence, the continuity equation is satisfied to one part in 2×10^5 in each control volume.

A gently ramping under-relaxation ($R = 0.05$) was used in the energy and species equations to speed convergence as well. Convergence criteria are that local changes in enthalpy, composition, and fraction solid and the average heat extracted from the left-hand wall were all less than 1×10^{-5} from one iteration to the next. Because these are relative-change convergence criteria, one must be careful when using variable under-relaxation to avoid false convergence. The values of the under-relaxation parameters for the energy and species equations upon convergence were always several orders of magnitude greater than the convergence criterion itself. The number of iterations to convergence varied between 35 and about 80 and was limited by the momentum equations, requiring more iterations when velocities were high. Time-step size varied with the problem being modeled ranging from 10^{-4} to 5×10^{-4}.

7. VERIFICATION OF THE MODEL

In order to check the model and code, simulations of previously published results from three different studies were undertaken. The first is for a one-dimensional pure diffusion solidification problem (i.e. $Ra = Rs = 0$) of Bennon and Incropera [25]; the second is for a two-dimensional solidification and convection problem of Ramachdran *et al.* [30]; and the third is for a solidification and convection problem of Voller *et al.* [3]. Bennon and Incropera use the continuum model [1] while Ramachdran *et al.* use a multi-region model [30] and Voller *et al.* use their two-phase model [3].

The first test case considered is a pure diffusion problem in which the left-hand wall of an impermeable and rigid box containing initially superliquidus aqueous ammonium chloride solution is held at a subsolidus temperature. The properties of the

Table 5. Assumed thermophysical properties of ammonium chloride and conditions for diffusion problem

Property	Units	Value
c_p	J kg^{-1} K^{-1}	2560
k	W m^{-1} K^{-1}	0.4305
ρ	kg m^{-3}	1078
D	m^2 s^{-1}	4.8×10^{-9}
μ	kg m^{-2} s^{-1}	1.3×10^{-3}
h_f	J kg^{-1}	3.138×10^{5}
T_{sol}	K	257.75
T_{liq}	K	306.0
T_m	K	633.6
T_w	K	223.0
C_0	—	0.700
C_{eut}	—	0.803
L	m	0.1
d	m	0.1
Dimensionless parameters		
Le		28
Pr		9.0
St		0.4344

system are given in Table 5 and are the same as those of Bennon and Incropera [25, 31] except that only one heat capacity was used in our calculation, thermal conductivity is the same in solid and liquid, and the simulation is for a pure binary eutectic phase diagram. Despite these differences, overall agreement between the two calculations was good. We used a uniform grid of 31 nodes in x and 6 nodes in y and a time step of 2×10^{-4}. Plotted in Fig. 4 are the dimensionless temperature ($\hat{T}=(T-T_{sol})/(T_0-T_{sol})$), the dimensionless composition of the liquid ($\hat{C}_{liq}=(C_{liq}-C_0)/(C_{eut}-C_0)$), and the fraction solid scalar fields at $\hat{t}=0.026$ ($t=240$ s). Total CPU time for the calculation was 50 s on the Cray 2 for 280 s of real time. The reader is referred to Bennon and Incropera [25] for direct comparison of the scalar fields. Bennon and Incropera [25] calculated the liquidus isotherm to be at $\hat{x}=0.67$; we find the liquidus isotherm to be at $\hat{x}=0.62$. Such differences between the two results might be expected given our use of a single heat capacity, single thermal conductivity, and pure binary eutectic phase diagram.

The second problem was that of the solidification and convection of pure tin carried out by Ramachdran *et al.* [30]. Pure molten tin is introduced into a mold with sidewall temperature maintained below the melting temperature in this single-component, pure tin system. Using the physical properties of molten tin and the same domain, boundary conditions, and equivalent dimensionless parameters as Ramachdran *et al.* [30], we obtained results in close agreement with theirs. We used a grid of 15 nodes in the horizontal and 30 nodes in the vertical and a time step of 5×10^{-4}. Plotted in Fig. 5 are the stream function and temperature fields at dimensionless time 0.27. Note that the domain is scaled to appear with unit aspect

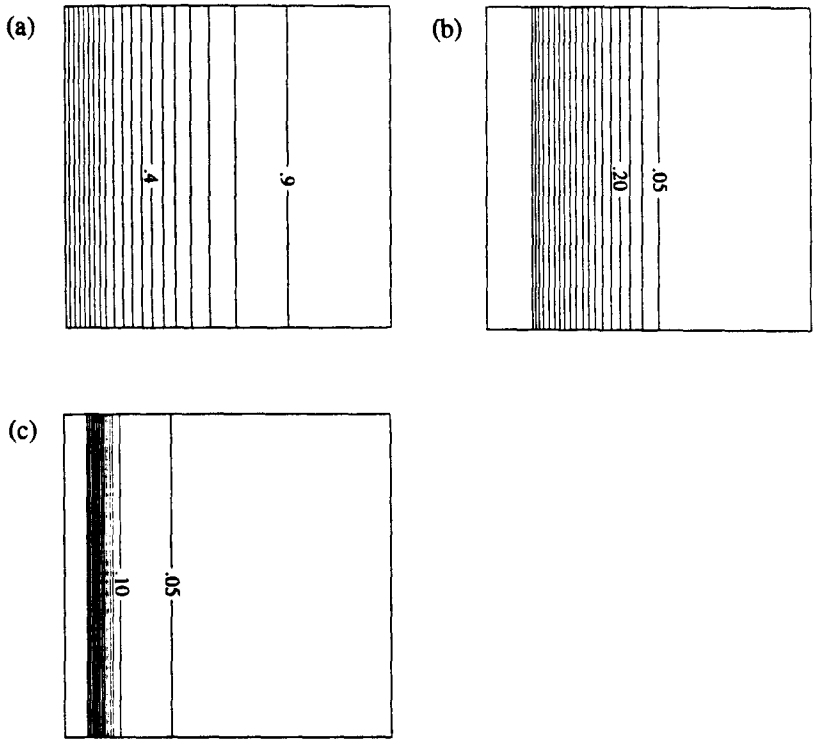

FIG. 4. Scalar fields for ammonium chloride one-dimensional solidification problem at $\hat{t}=0.026$. (a) Isotherms: contour interval is 0.08, $\hat{T}_{max}=0.99$. (b) Isopleths of $\hat{C}_{liq}$: contour interval is 0.05, $C_{eut}=0.803$, $C_0=0.70$. (c) Isopleths of fraction solid (f_s): contour interval is 0.05, $f_{s\,max}=1$.

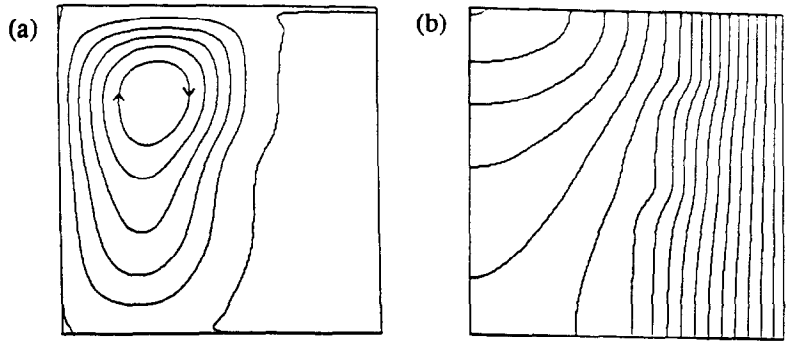

FIG. 5. Scalar fields for the solidification and convection of pure tin at $\hat{t} = 0.27$. (a) Dimensionless stream function (ψ) of the mixture: $\psi_{min} = -1.06$, contour interval is 0.15. (b) Isotherms of $\hat{T}$ field: $\hat{T}_{max} = 0.659$ in upper left-hand corner and the contour interval is 0.10. The $\hat{T}$ field shows the conductive profile in the solid and the convective profile in the liquid region. Due to differences in the definition of $\hat{T}$, the isotherms should be compared to those of Ramachdran *et al.* [30] for their general shape only and not for the actual values of $\hat{T}$.

ratio as done by Ramachdran *et al.* [30] even though the calculation is carried out in a domain which is 2.2 times taller than it is wide. We calculated the minimum dimensionless stream function (ψ_{min}) to be -1.057, while Ramachdran *et al.* [30] report ψ_{min} equal to -1.0. Because of differences in the definition of dimensionless temperature, the isotherms in Fig. 5(b) should be compared to those of Ramachdran *et al.* [30] for general character only and not for specific values of dimensionless temperature. The two knees (stairstep pattern) in the isotherms of Fig. 5(b) near the solid–melt interface are sensitive to the number of nodes, with smoother shaped isotherms resulting when the resolution is increased. The location of the solid–melt interface can be inferred from the stream function plot. Our calculation has slightly underpredicted the amount of solidification relative to Ramachdran *et al.* [30] at the same dimensionless time, perhaps due to our use of a single thermal conductivity. Overall agreement between our model and that of Ramachdran *et al.* [30] is good for this single-component test problem. Refer to Figs. 4 and 5 of Ramachdran *et al.* [30] for direct comparison.

The third problem investigated was one of the solidification and convection examples presented by Voller *et al.* [3]. In the problem, a sidewall of a container of superliquidus ammonium chloride solution is held at a temperature below the liquidus but above the solidus temperature. For these conditions, the fraction solid never reaches unity in the domain and the end-product is mush. The additional properties as given in ref. [3] of aqueous ammonium chloride necessary for this convection problem are listed in Table 6 along with the values of the dimensionless parameters we used; other properties are as given in Table 5. We used a uniform grid of 31 nodes in x and y and a time step of 2.5×10^{-4}. Figure 6 shows plots of the stream function and fraction solid at $\hat{t} = 0.19$ ($t = 250$ s). Total CPU time for this calculation was about 12 000 s on the Cray X-MP. Overall agreement with Voller *et al.* [3] is generally good, with some differences. The maximum stream function (ψ_{max}) is

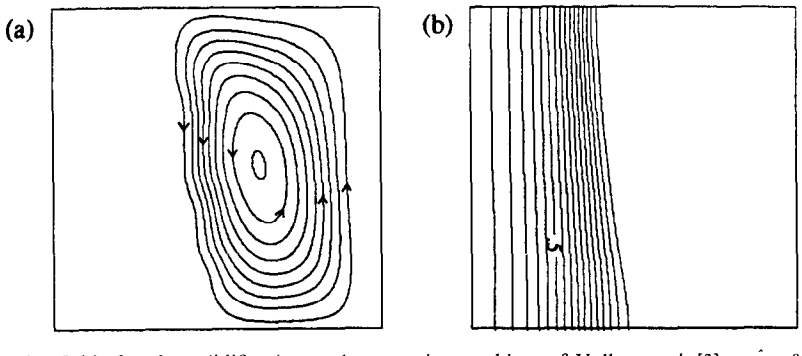

FIG. 6. Scalar fields for the solidification and convection problem of Voller *et al.* [3] at $\hat{t} = 0.19$ ($t = 250$ s). (a) Stream function (ψ) for the velocity of the mixture: $\psi_{max} = 1.6 \times 10^{-3}$ m^2 s^{-1} as compared with 1.3×10^{-3} m^2 s^{-1} calculated by Voller *et al.* (b) Fraction solid (f_s) field. The $f_s = 0.5$ isopleth is at $\hat{x} = 0.25$ at a height of $\hat{y} = 0.5$. Voller *et al.* [3] show the $f_s = 0.5$ isopleth at $\hat{x} = 0.28$ at the same elevation.

Table 6. Additional thermophysical properties and assumed dimensionless parameters for the solidification and convection problem

Property	Units	Value
α	K^{-1}	4×10^{-4}
β	—	0.025
K	m^2	5×10^{-10}
L	m	0.025
d	m	0.025
T_0	K	600
T_∞	K	400
C_0	—	0.10
Dimensionless parameters		
Ra		1×10^{6}
Rs		2×10^{6}
Pr		9.0
Le		28
Da		8×10^{-10}
St		3.5

Table 7. Thermophysical properties and dimensionless groups for the Di80 numerical experiment (see Table 2 for additional information)

Property	Units	Value
c_p	$J\,kg^{-1}\,K^{-1}$	1006
h_{sol}	$J\,kg^{-1}$	1.557×10^{6}
h^*_{liq}	$J\,kg^{-1}$	1.901×10^{6}
h^*_f	$J\,kg^{-1}$	3.310×10^{5}
h_f	$J\,kg^{-1}$	3.547×10^{5}
T_0	K	1610
Dimensionless parameters		
Ra		1×10^{6}
Rs		2×10^{6}
Pr		1000
Le		100
Da		10^{-10}
St		0.181

equal to 1.3×10^{-3} m^2 s^{-1} in their calculation and agrees well with our value of 1.6×10^{-3} m^2 s^{-1}. The early stages of a compositionally-driven recirculating flow shown in ref. [3] are absent in our results at 250 s. In addition, we found better agreement between the flow fields in the two models when we used $Da = 8\times10^{-10}$ rather than the value 8×10^{-7} apparently used by Voller *et al.* The location of the 0.5 fraction solid isopleth agreed between the two models to within about 15%. These discrepancies most likely result from our use of a slightly different model (continuum [1] vs two-phase [3]) and from our use of values of dimensionless parameters only approximately equivalent to those in ref. [3]. We refer the reader to Voller *et al.* [3] for direct comparison of the fraction solid and stream function fields.

8. EXAMPLE CALCULATION OF SOLIDIFICATION OF SILICATE MELT

8.1. *Di80*

In order to show the capabilities of our pure binary eutectic model for solidification and convection of silicate melt, we present in this section the results of one numerical experiment of the solidification of Di80 melt. The model domain and boundary conditions are shown in Fig. 1. The left-hand wall of a two-dimensional container of Di80 with uniform temperature equal to 1337°C is suddenly cooled to subsolidus temperature equal to 1265°C.

The physical conditions and dimensionless groups for the Di80 experiment are given in Table 7. The thermophysical properties are well constrained by experimental measurements [32, 33]. The dimensionless numbers, *Ra*, *Rs*, and *Le* are restricted, for practical reasons, to values not strictly correct for basaltic magma. Specifically, the magnitudes of *Ra* and *Rs* imply a very small model domain, while the magnitude of *Le* exaggerates the importance of chemical diffusion. The Darcy number chosen here is rather arbitrary, as we know of no measurements of K_0 for Di–An.

A 31×31 uniform grid with time step equal to 1×10^{-4} was used. The simulation required about 10000 s on a Cray X-MP. A verification run with a 51×51 uniform grid and time-step of 5×10^{-5} gave results which differed in average enthalpy, average temperature, and average fraction solid by less than 1% at dimensionless time 0.04. Downward flow along the left-hand wall begins due to the developing thermal gradients in the container at the same time as melt solidifies in regions near the wall. Figures 7–9 show the dimensionless velocity of the liquid, dimensionless temperature, normalized dimensionless composition of the mixture, and the fraction solid fields at three different times.

The following discussion refers to Figs. 7–9. The velocity of the liquid vector diagrams show the vigorous convection early in the evolution and the very sluggish convection which occurs at late times when most of the domain is mush. The velocity of the solid matrix is zero and the permeability is assumed isotropic throughout. Note the large temperature drop which occurs across the solid and mush region along the left-hand wall at $\hat{t} = 0.01$. Much of the negative buoyancy associated with the cold wall is locked up in mush with permeability too small to allow significant convection. Later in the evolution, the mush region extends across the entire domain and convective velocities are small. It is important to note that the Rayleigh number based on the width of the domain may be large, but as solidification proceeds, convective vigor decreases drastically as the flow becomes dominated by porous media convection.

The mixture composition field (C^*), where $C^* = (C - C_{min})/(C_{max} - C_{min})$, shows very interesting segre-

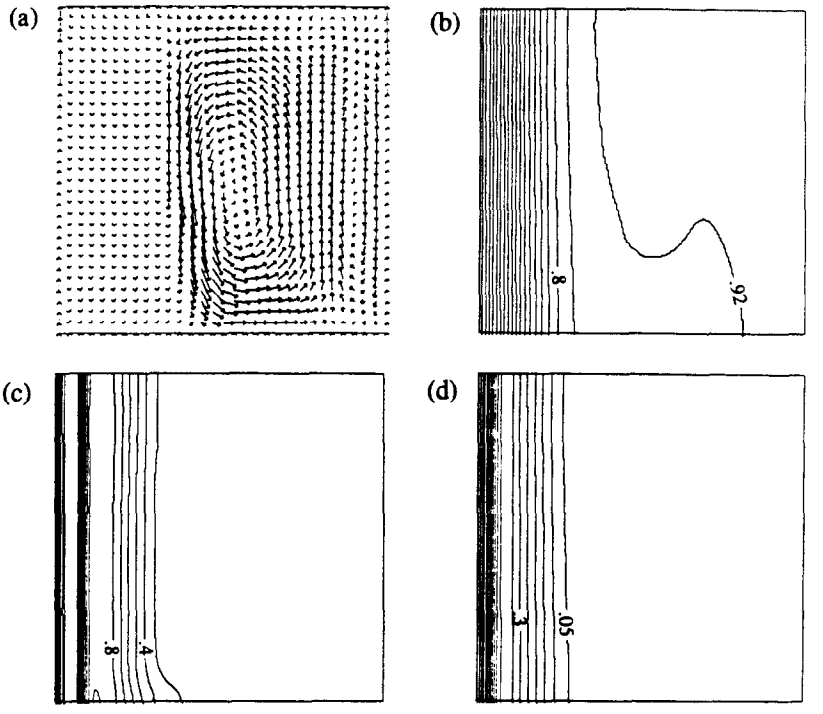

FIG. 7. Velocity and scalar fields for Di80 solidification and convection problem at $\hat{t} = 0.01$. (a) Velocity of the liquid: $\hat{v}_{max} = 170$. (b) Isotherms: contour interval is 0.06, $\hat{T}_{max} = 0.98$. Note the large temperature drop across the solid along the left-hand wall and the convective temperature profile in the remainder of the domain. (c) Isopleths of dimensionless normalized mixture composition C^* ($C^* = (C - C_{min})/(C_{max} - C_{min})$): contour interval is 0.1. The maximum and minimum mixture compositions are: $C_{max} = 0.2028$; $C_{min} = 0.1989$. A region of mush enriched in eutectic composition melt ahead of the solidification front can be seen as a ridge to the left of the labeled 0.8 isopleth. The overall differences in mixture composition produced by the solidification process are small. (d) Isopleths of fraction solid: $f_{smin} = 0.0$, $f_{smax} = 1$. Along the left-hand wall, $f_s = 1$; outside of that is a thin region of mush; the rest of the domain is liquid.

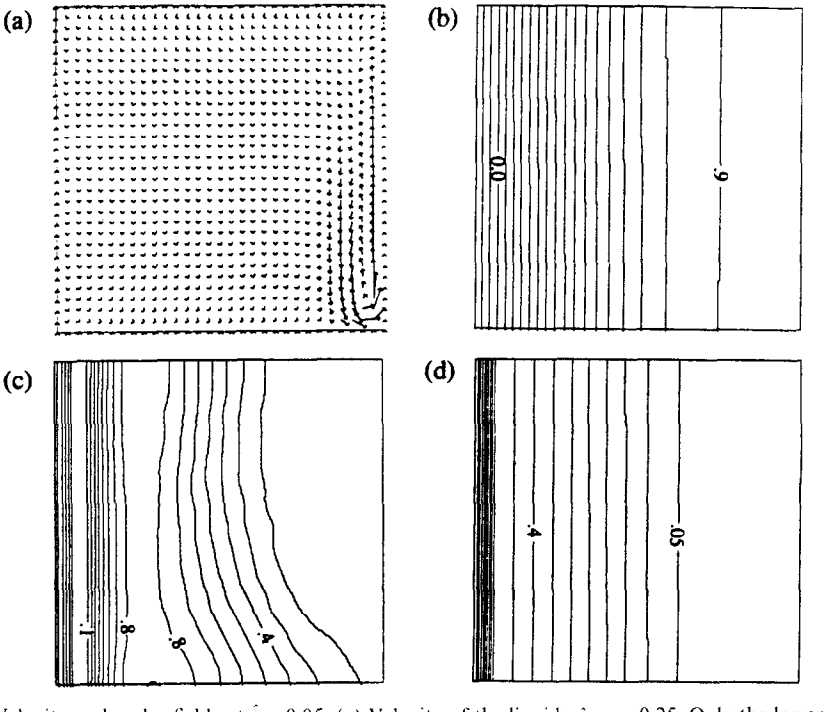

FIG. 8. Velocity and scalar fields at $\hat{t} = 0.05$. (a) Velocity of the liquid: $\hat{v}_{max} = 0.25$. Only the lower right-hand corner of the domain contains liquid capable of significant convection. (b) Isotherms: contour interval is 0.056, $\hat{T}_{max} = 0.95$. Temperature profiles are nearly straight and unperturbed by the weak convection. (c) Isopleths of C^*: contour interval is 0.1; $C_{max} = 0.2030$; $C_{min} = 0.1995$. The enriched region is moving to the right and widening. The corresponding depleted region occurs near the left-hand wall just inside the solidification front (see the 0.1 isopleth). (d) Isopleths of fraction solid: $f_{smin} = 0.006$, $f_{smax} = 1$. A narrow region with $f_s = 1$ exists along the left-hand wall while the rest of the domain is mush.

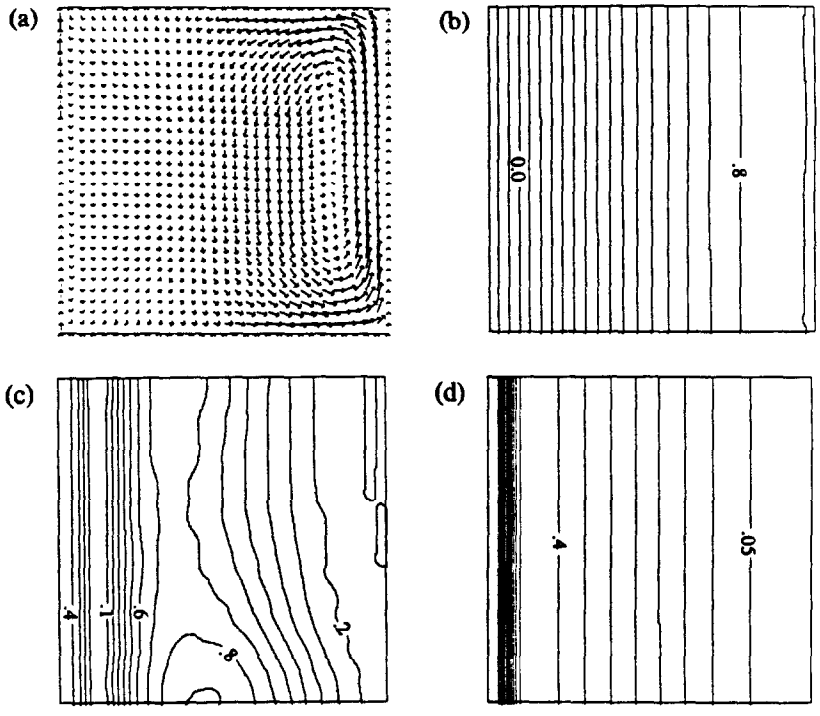

FIG. 9. Velocity and scalar fields at $\hat{t} = 0.10$. (a) Velocity of the liquid: $\hat{v}_{max} = 0.005$. Convection in the domain is very weak. (b) Isotherms: contour interval is 0.054, $\hat{T}_{max} = 0.91$. (c) Isopleths of C^*: contour interval is 0.1; $C_{max} = 0.2032$; $C_{min} = 0.2004$. Enriched and depleted regions are further to the right, and the overall variation of mixture composition is small. (d) Isopleths of fraction solid: $f_{smin} = 0.04$, $f_{smax} = 1$. Solid regions exist along the left-hand wall while the rest of the domain is mush.

gation patterns. At early time, there is a band of low values (a valley) near the cold wall and a region of higher values (a ridge) just outward from it. The valley represents areas where the composition of the liquid is eutectic. It appears as a low point because there is about 50% solid there, and the mixture composition takes into account the 50% of pure Di present. Toward the wall from this valley, the value of C^* increases up to the value of C_0, the initial bulk composition where $f_s = 1$. Toward the right from the valley, C^* increases into a broad ridge. This ridge is caused by the expulsion of An-rich melt during the solidification of pure Di at temperatures above the solidus and below the liquidus. The fraction solid of pure Di in this region is not large enough to counteract the effect on C^* of the rejected solute (An-rich melt). This valley and ridge pattern is observed throughout the evolution. The edge of the ridge appears to be eroded by convection at later times and its shape reflects the sense of even very weak convection. It should be emphasized that the overall magnitude of the mixture compositional differences is very small, but the segregation pattern is none the less interesting and certainly caused by the solidification process.

The evolution of the fraction solid field shows the growth of the mush region. The completely solidified region along the wall can be seen clearly in Fig. 9(d). Note the steep gradient in fraction solid which occurs at the solidus temperature. The mush region extends across the whole domain by $\hat{t} = 0.10$ (Fig. 9).

9. CONCLUSIONS

The phase change and convection of viscous pure binary eutectic silicate melt can be numerically modeled by the same methods as have been successfully applied to metallurgical systems. The pure binary eutectic character is accommodated by defining a mixed solid of eutectic composition and explicitly considering its enthalpy of fusion. The large viscosity of silicate melt causes slow convergence of the iterative SIMPLER algorithm. This problem can be overcome by the use of variable under-relaxation in the momentum equations. Our model has been tested and agrees substantially with the work of other researchers. An example simulation of the solidification and convection of Di80 demonstrates the capabilities of the model and at the same time shows that solidification decreases convective vigor by (1) controlling heat flow along the cold wall and (2) by virtue of producing a solid matrix which forces porous media flow to occur. Interesting transient compositional segregation patterns form during the evolution of the solidification systems.

We emphasize in closing the many extensions to the model which are possible and list some of them here

in order of increasing difficulty: (1) extension to three dimensions; (2) use of complex and non-linear viscosity and other transport property functions; (3) implementation of more realistic multicomponent systems rather than two-component systems; (4) application of thermodynamic phase equilibria rather than the local thermodynamic equilibrium approximation; and (5) inclusion of crystal nucleation and growth rate functions. Extensions 1–3 are straightforward; extensions 4 and 5 are inseparable and considerably more involved than 1–3. However, in theory, all of these extensions can be accommodated within the framework of the present model to lead to more accurate simulations of complex phase-change phenomena.

Acknowledgements—This work was supported by NSF (EAR88-16103) and NASA (NAGW-1452) to FJS. We thank David A. Yuen for discussion and acknowledge the helpful staffs of MSI (University of Minnesota Supercomputer Institute) and NAS (NASA–Ames Research Center) where these computations were performed.

REFERENCES

1. W. D. Bennon and F. P. Incropera, A continuum model for momentum, heat and species transport in binary solid–liquid phase change systems—I. Model formulation, *Int. J. Heat Mass Transfer* **30,** 2161–2170 (1987).
2. C. Beckermann and R. Viskanta, Double-diffusive convection during dendritic solidification of a binary mixture, *PhysicoChem. Hydrodyn.* **10,** 195–213 (1988).
3. V. R. Voller, A. D. Brent and C. Prakash, The modelling of heat, mass and solute transport in solidification systems, *Int. J. Heat Mass Transfer* **32,** 1719–1731 (1989).
4. S. V. Patankar, *Numerical Heat Transfer and Fluid Flow*, 197 pp. Hemisphere, Washington, DC (1980).
5. C. A. J. Fletcher, *Computational Techniques for Fluid Dynamics*, Vol. II, 486 pp. Springer, Berlin (1988).
6. W. D. Bennon and F. P. Incropera, A continuum model for momentum, heat and species transport in binary solid–liquid phase change systems—II. Application to solidification in a rectangular cavity, *Int. J. Heat Mass Transfer* **30,** 2171–2187 (1987).
7. M. S. Christenson, W. D. Bennon and F. P. Incropera, Solidification of an aqueous ammonium chloride solution in a rectangular cavity—II. Comparison of predicted and measured results, *Int. J. Heat Mass Transfer* **32,** 69–79 (1989).
8. M. E. Thompson and J. Szekely, Mathematical and physical modelling of double-diffusive convection of aqueous solutions crystallizing at a vertical wall, *J. Fluid Mech.* **187,** 409–433 (1988).
9. J. S. Turner and L. B. Gustafson, Fluid motions and compositional gradients produced by crystallization or melting at vertical boundaries, *J. Volcanol. Geotherm. Res.* **11,** 93–125 (1981).
10. H. E. Huppert, R. S. J. Sparks, J. R. Wilson, M. A. Hallworth and A. M. Leitch, Laboratory experiments with aqueous solutions modelling magma chamber processes—II. Cooling and crystallization along inclined planes. In *Origins of Igneous Layering* (Edited by I. Parsons), pp. 539–568. D. Reidel, Holland (1987).
11. M. K. Smith, Thermal convection during the directional solidification of a pure liquid with variable viscosity, *J. Fluid Mech.* **188,** 547–570 (1988).
12. B. D. Marsh, On convective style and vigor in sheet-like magma chambers, *J. Petrology* **30,** 479–530 (1989).
13. M. G. Worster, H. E. Huppert and R. S. J. Sparks, Convection and crystallization in magma cooled from above, *Earth Planet. Sci. Lett.*, in press.
14. C. M. Oldenburg, F. J. Spera, D. A. Yuen and G. Sewell, Dynamic mixing in magma bodies: theory, simulations, and implications, *J. Geophys. Res.* **94,** 9215–9236 (1989).
15. F. J. Spera, C. M. Oldenburg and D. A. Yuen, Magma zonation: effects of chemical buoyancy and diffusion, *Geophys. Res. Lett.* **16,** 1387–1390 (1989).
16. C. R. Carrigan, The magmatic Rayleigh number and time dependent convection in cooling lava lakes, *Geophys. Res. Lett.* **14,** 915–918 (1987).
17. H. M. Iyer, Geophysical evidence for the locations, shapes and sizes, and internal structures of magma chambers beneath regions of Quaternary volcanism, *Phil. Trans. R. Soc. Lond. A* **310,** 473–510 (1984).
18. A. H. Lachenbruch and J. H. Sass, Heat flow in the United States and the thermal regime of the crust, *Geophys. Monogr. Ser.* **20,** 626–675 (1977).
19. W. Hildreth, The Bishop Tuff: evidence for the origin of compositional zonation in silicic magma chambers, *Geol. Soc. America Special Paper* **180,** 75 pp. (1979).
20. J. A. Crisp, Rates of magma emplacement and volcanic output, *J. Volcanol. Geotherm. Res.* **20,** 177–211 (1984).
21. H. R. Shaw, Viscosities of magmatic silicate liquids: an empirical method of prediction, *Am. J. Sci.* **272,** 870–893 (1972).
22. A. B. Metzner, Rheology of suspensions in polymeric liquids, *J. Rheology* **29,** 739–760 (1985).
23. C. M. Oldenburg and F. J. Spera, Simulation of phase change and convection in magma bodies. In *Heat Transfer in Earth Science Studies* (Edited by C. Carrigan and T. Y. Chu), ASME HTD Vol. 149, pp. 35–42 (1990).
24. G. O. Roberts, Fast viscous Benard convection, *Geophys. Astrophys. Fluid Dynam.* **12,** 235–272 (1979).
25. W. D. Bennon and F. P. Incropera, Numerical analysis of binary solid–liquid phase change using a continuum model, *Numer. Heat Transfer* **13,** 277–296 (1988).
26. S. V. Patankar and D. B. Spalding, A calculation procedure for heat, mass and momentum transfer in three-dimensional parabolic flows, *Int. J. Heat Mass Transfer* **15,** 1787–1806 (1972).
27. S. V. Patankar, A calculation procedure for two-dimensional elliptic situations, *Numer. Heat Transfer* **4,** 409–425 (1981).
28. J. P. Van Doormaal and G. D. Raithby, Enhancements of the SIMPLE method for predicting incompressible fluid flows, *Numer. Heat Transfer* **7,** 147–163 (1984).
29. P. F. Galpin and G. D. Raithby, Numerical solution of problems in incompressible fluid flow: treatment of the temperature–velocity coupling, *Numer. Heat Transfer* **10,** 105–129 (1986).
30. N. Ramachdran, J. P. Gupta and Y. Jaluria, Thermal and fluid flow effects during solidification in a rectangular enclosure, *Int. J. Heat Mass Transfer* **25,** 187–194 (1982).
31. W. D. Bennon and F. P. Incropera, Numerical simulation of binary solidification in a vertical channel with thermal and solutal mixed convection, *Int. J. Heat Mass Transfer* **31,** 2147–2160 (1987).
32. R. A. Robie, B. S. Hemingway and J. R. Fisher, Thermodynamic properties of minerals and related substances at 298.15 K and 1 bar (10^5 pascals) pressure and at higher temperatures, *U.S. Geol. Surv. Bull.* **1452,** 456 pp. (1979).
33. D. F. Weill, R. Hon and A. Navrotsky, The igneous system $CaMgSi_2O_6$–$CaAl_2Si_2O_8$–$NaAlSi_3O_8$: variations on a classic theme by Bowen. In *Physics of Magmatic Processes* (Edited by R. B. Hargraves), pp. 49–92. Princeton University Press, Princeton, New Jersey (1980).

APPENDIX

The composition of the mixture in a binary system is given by

$$C = f_s C_s + (1 - f_s) C_l. \tag{A1}$$

For supersolidus mush regions ($f_s < (T_{liq} - T_{sol})/(T_m - T_{sol})$) in the pure binary eutectic system shown in Fig. 2 with bulk composition C_0, the liquid and solid compositions are given by

$$C_l = \frac{C}{(1 - f_s)} \tag{A2}$$

$$C_s = 0. \tag{A3}$$

At the solidus temperature ($f_s \geq (T_{liq} - T_{sol})/(T_m - T_{sol})$), the liquid and solid compositions are

$$C_l = C_{eut} \tag{A4}$$

$$C_s = \left(f_s - \frac{T_{liq} - T_{sol}}{T_m - T_{sol}} \right) C_{eut}. \tag{A5}$$

Substituting equations (A4) and (A5) into equation (A1), one derives the equation for the composition of the mixture at and below the solidus temperature

$$C = f_s \left(f_s - \frac{T_{liq} - T_{sol}}{T_m - T_{sol}} \right) C_{eut} + (1 - f_s) C_{eut}. \tag{A6}$$

MODELISATION NUMERIQUE DE LA SOLIDIFICATION ET LA CONVECTION DANS UN SYSTEME BINAIRE EUTECTIQUE VISQUEUX

Résumé—On modélise numériquement la solidification et la convection d'un système stilicate binaire eutectique diopside–anorthite (Di–An). On utilise une enthalpie de fusion pondérée par la masse pour tenir compte de la seconde phase solide (An) qui cristallise à la température du solidus. On utilise une relaxation pour aider la convergence des équations de quantité de mouvement dans l'application de l'algorithme SIMPLER utilisé pour résoudre les équations bidimensionnelles de bilan. Des expériences numériques de solidification de Di80 montrent qu'un grand saut de température qui se produit à travers les régions de solide et de boue fait décroitre l'intensité de la convection dans le liquide. Des configurations intéressantes de ségrégation sont produites pendant la solidification du Di80.

NUMERISCHE MODELLIERUNG DER VERFESTIGUNG UND KONVEKTION IN EINEM VISKOSEN REINEN ZWEISTOFF-EUTEKTIKUM

Zusammenfassung—Verfestigung und Konvektion eines reinen binären eutektischen Silikat-Systems aus Diopside–Anorthite (Di–An) werden numerisch modelliert. Eine massenbezogene Schmelzenthalpie wird zur Berücksichtigung der zweiten festen Phase (An) benutzt, die bei Erreichen der Solidus-Temperatur kristallisiert. Zur Unterstützung der Konvergenz der Impuls-Gleichungen in der Realisierung des SIMPLER-Algorithmus, der zur Lösung der zweidimensionalen Kontinuums-Erhaltungsgleichungen benutzt wird, verwendeten die Autoren variable Unterrelaxation. Die numerische Untersuchung der Kristallisation von Di80-Schmelze zeigt, daß quer durch den Feststoff ein großer Temperatur-Abfall auftritt und außerdem Erweichungszonen, welche die Konvektionsintensität in der Flüssigkeit verringern. Bei der Kristallisation von Di80-Schmelze wurden interessante Ausseigerungsmuster erzeugt.

ЧИСЛЕННОЕ МОДЕЛИРОВАНИЕ ПРОЦЕССОВ ЗАТВЕРДЕВАНИЯ И КОНВЕКЦИИ В ВЯЗКОЙ БИНАРНОЙ ЭВТЕКТИЧЕСКОЙ СИСТЕМЕ

Аннотация—Проводится численное моделирование процессов затвердевания и конвекции бинарной эвтектической системы диопсид–анортит (Di–An). Усредненная по массе энтальпия плавления используется для учета второй твердой фазы (An), кристаллизующейся при температуре солидуса. При численном счете используется нижняя релаксация, что способствует сходимости уравнений сохранения количества движения при введении алгоритма SIMPLER, применяемого для решения двумерных уравнений сохранения континуума. Численные эксперименты по затвердеванию расплава Di80 показывают, что на твердых и двухфазных участках происходит значительный перепад температуры, что приводит к снижению интенсивности конвекции в жидкости. Получены интересные картины композиционной сегрегации в процессе затвердевания Di80.